



Cite this: *J. Mater. Chem. A*, 2024, 12, 21864

# Interface engineering and oxygen vacancies derived from plasma-treated Cu<sub>2</sub>O synergistically enhancing electrocatalytic CO<sub>2</sub>-to-C<sub>2+</sub> conversion†

Lei Wang,<sup>‡,ab</sup> Xue Yao,<sup>‡,c</sup> Subhajit Jana,<sup>‡,a</sup> Yongzan Zhou,<sup>‡,a</sup> Chunlan Qin,<sup>d</sup> Hongwei Shou,<sup>d</sup> Youchao Teng,<sup>id a</sup> Ning Chen,<sup>e</sup> Lidong Zhang,<sup>id c</sup> Chandra Veer Singh,<sup>id \*cf</sup> Zhongchao Tan<sup>\*ag</sup> and Yimin A. Wu<sup>id \*abh</sup>

Electrocatalytic CO<sub>2</sub> reduction (ECR) into value-added chemicals and fuels helps tackle the challenges of the energy crisis and global warming. However, this strategy relies heavily on the rational design of catalysts with high selectivity and activity towards C<sub>2+</sub> products. Herein, we introduce a dual-engineering strategy using plasma-treated Cu<sub>2</sub>O to synergistically enhance the material's catalytic performance for CO<sub>2</sub>-to-C<sub>2+</sub> conversion. We demonstrate that well-controlled plasma reduction treatment in an Ar/H<sub>2</sub> atmosphere can yield stable Cu<sub>2</sub>O–Cu catalysts (Cu<sub>2</sub>O–Ar/H<sub>2</sub>) with Cu<sup>0</sup>/Cu<sup>+</sup> interfaces, abundant grain boundaries, and a high density of oxygen vacancies. Cu<sub>2</sub>O–Ar/H<sub>2</sub> delivers an impressive 81.2% faradaic efficiency for C<sub>2+</sub> products at an industrial current density of 100 mA cm<sup>−2</sup>. Performance comparisons show that plasma pre-reduction treatment samples outperform the *in situ* reduced Cu<sub>2</sub>O sample during ECR. Theoretical calculations reveal that the well-defined Cu<sup>0</sup>/Cu<sup>+</sup> interfaces optimize intermediate adsorption and the oxygen vacancies provide multiple active sites for C–C coupling. This work establishes a correlation between plasma treatment-generated active sites and high C<sub>2+</sub> product selectivity. Our work also demonstrates that this facile, scalable, standardized and controllable material preparation method can effectively promote the large-scale application of high-activity ECR catalysts.

Received 20th May 2024  
Accepted 15th July 2024

DOI: 10.1039/d4ta03492a

rsc.li/materials-a

## 1 Introduction

Electrocatalytic CO<sub>2</sub> reduction (ECR) into high-value chemicals and feedstocks using renewable electricity offers an elegant solution for closing the carbon cycle, addressing global environmental issues, and meeting growing energy demands.<sup>1,2</sup>

However, the potential of this technology heavily relies on the development of highly active and selective electrocatalysts.<sup>3,4</sup> Although other metals such as Ag and Sn have achieved highly selective C<sub>1</sub> products, such as CO and formate,<sup>5,6</sup> achieving high selectivity for C<sub>2+</sub> products on Cu-based catalysts remains highly challenging due to their sluggish multiple proton-coupled electron transfer (PCET) processes in C–C coupling and the competitive hydrogen evolution reaction (HER).<sup>7</sup> Therefore, there is an urgent need to develop highly efficient and active catalysts with scalable synthesis methods that can enhance selectivity towards C<sub>2+</sub> products.

To enhance ECR to C<sub>2+</sub> conversion selectivity, substantial efforts have focused on the rational design of copper-based catalysts, including morphology,<sup>8</sup> oxide-derived copper (OD-Cu),<sup>9</sup> interfacial structures,<sup>10,11</sup> and alloying<sup>12,13</sup> strategies. In particular, OD-Cu has been reported with excellent C<sub>2+</sub> selectivity,<sup>4</sup> garnering widespread research interest. However, for OD-Cu, the active Cu<sup>+</sup> species inevitably undergoes electrochemical reduction to bulk metallic Cu at high current densities,<sup>14</sup> leading to poor selectivity for C<sub>2+</sub> products. This poses a significant challenge for the effective utilization of OD-Cu. Thus, unconventional and feasible strategies for stabilizing the active Cu<sup>+</sup> species at reduction potentials during actual CO<sub>2</sub>

<sup>a</sup>Department of Mechanical and Mechatronics Engineering, University of Waterloo, Waterloo, Ontario N2L 3G1, Canada. E-mail: yimin.wu@uwaterloo.ca

<sup>b</sup>Waterloo Institute for Nanotechnology, University of Waterloo, Waterloo, Ontario N2L 3G1, Canada

<sup>c</sup>Department of Materials Science and Engineering, University of Toronto, Toronto, Ontario M5S 3E4, Canada. E-mail: chandraveer.singh@utoronto.ca

<sup>d</sup>National Synchrotron Radiation Laboratory, University of Science and Technology of China, Hefei 230029, P. R. China

<sup>e</sup>Canadian Light Source, Saskatoon, SK S7N 2V3, Canada

<sup>f</sup>Department of Mechanical and Industrial Engineering, University of Toronto, Toronto, Ontario M5S 3G8, Canada

<sup>g</sup>Eastern Institute of Technology, No. 568 Tongxin Road, Zhenhai District, Ningbo, Zhejiang, 315200, China. E-mail: ztan@eitech.edu.cn

<sup>h</sup>Department of Chemistry, University of Waterloo, Waterloo, Ontario N2L 3G1, Canada

† Electronic supplementary information (ESI) available. See DOI: <https://doi.org/10.1039/d4ta03492a>

‡ Equal contributions.

reduction processes is necessary. Research results indicate that abundant nanograin boundaries can enhance the stability of catalyst morphology and  $\text{Cu}^0/\text{Cu}^+$  interfaces at high polarization and high current density, preventing catalyst reconstruction and improving the catalytic stability.<sup>15</sup> Moreover, nanograin boundaries and the  $\text{Cu}^0/\text{Cu}^+$  interface can increase  $^*\text{CO}$  adsorption strength, promoting  $\text{CO}$ – $\text{CO}$  coupling toward  $\text{C}_{2+}$  products.<sup>16,17</sup> Therefore, constructing intricate structures assembled with abundant nanograin boundaries and  $\text{Cu}^0/\text{Cu}^+$  interfaces in Cu-based catalysts is promising for achieving efficient ECR to  $\text{C}_{2+}$  products.

In addition, oxygen vacancies, as a well-known defect, are widely employed to tailor the properties of catalysts.<sup>18–20</sup> For example, due to their weakly bound electrons, oxygen vacancies serve as excellent Lewis base sites to enhance the binding affinities of key intermediates (such as  $^*\text{CO}$  and  $^*\text{COH}$ ), thereby promoting the production of  $\text{C}_2$ .<sup>21</sup> Moreover, a higher concentration of oxygen vacancies near the active sites is favorable for activating  $\text{CO}_2$  molecules, lowering the reaction barrier for targeted products.<sup>22</sup> Therefore, integrating oxygen vacancies with grain boundaries and interface engineering is likely to modulate the surface electronic structure and concentration of active sites, accelerating reaction kinetics. However, effectively constructing oxygen vacancies and interface structures on the catalyst surface is highly challenging. A deeper understanding of the synergistic interaction between oxygen vacancies and interface structures will provide valuable guidance for the rational design of catalysts.

Plasma treatment, as a facile and scalable technique, has been introduced to selectively activate catalysts, due to its ability to rapidly alter the surface chemical state of catalysts at room temperature,<sup>23</sup> create defect structures,<sup>24</sup> or embed heteroatoms<sup>25</sup> to improve reactivity. For example, Cu surfaces treated with  $\text{O}_2$  plasma exhibit higher ethylene selectivity than those treated with  $\text{H}_2$  plasma. The activity enhancement may originate from the presence of  $\text{Cu}^+$ .<sup>26</sup> Cuenya's group reported that  $\text{O}_2$  plasma treatment gives rise to specific defect sites and stable subsurface oxygen species inside Cu nanocubes, which are key to achieving high activity and ethylene selectivity.<sup>27</sup> Additionally, Kang's group indicated that oxygen-plasma-assisted nitrogen doping on CuO can achieve high  $\text{C}_{2+}$  product selectivity, with enhanced activity attributed to the oxygen vacancies and grain boundary defects generated by  $\text{N}_2$  plasma radicals on CuO.<sup>24</sup> These studies suggest that plasma treatment, as an effective surface treatment method, can precisely control active sites under different atmospheres.<sup>28,29</sup> Nevertheless, whether plasma treatment can be used to synergistically construct oxygen vacancies and  $\text{Cu}^+/\text{Cu}^0$  interface structures on the metal oxide catalyst surface has yet to be investigated.

In this study, we employ plasma treatment under different atmospheres as a dual-engineering strategy to couple oxygen vacancies and interface structures, aiming to enhance the activity of the ECR catalysts. Plasma treatment in an  $\text{Ar}/\text{H}_2$  environment results in the reduction of grain-boundary-rich  $\text{Cu}_2\text{O}$ , creating active interfaces of  $\text{Cu}^0/\text{Cu}^+$  interface structures and abundant oxygen vacancies. Compared to original  $\text{Cu}_2\text{O}$  and  $\text{Cu}_2\text{O}$  treated under an  $\text{Ar}/\text{O}_2$  atmosphere ( $\text{Cu}_2\text{O}-\text{Ar}/\text{O}_2$ ), the

coordinated interaction between  $\text{Cu}^0/\text{Cu}^+$  and oxygen vacancies from  $\text{Cu}_2\text{O}-\text{Ar}/\text{H}_2$  contributes to enhanced catalytic activity for  $\text{C}_{2+}$  products. DFT calculations indicate that  $\text{Cu}_2\text{O}-\text{Ar}/\text{H}_2$  is more favorable for  $^*\text{OHCCO}$  intermediate adsorption, promoting the conversion of  $\text{C}_{2+}$  products. As a result, the  $\text{Cu}_2\text{O}-\text{Ar}/\text{H}_2$  sample achieves a faradaic efficiency of 81.4% for  $\text{C}_{2+}$  products at a current density of  $100 \text{ mA cm}^{-2}$ . This study reveals the mechanism by which plasma treatment enhances catalyst activity, advancing the development of ECR to  $\text{C}_{2+}$  products.

## 2 Experimental section

### 2.1 Materials

A  $\text{Cu}_2\text{O}$  target was purchased from AJA International Inc, USA. Potassium hydroxide (KOH) and ultrapure water ( $18 \text{ M}\Omega \text{ cm}$ ) were obtained from the University of Waterloo Chemical Store. Carbon paper (Freudenberg H15C13) and a Fumasep FAB-PK-130 membrane were purchased from a fuel cell store, USA. Argon and  $\text{CO}_2$  gas were provided by Linde Gas, Canada.

### 2.2 Synthesis of electrocatalysts

**2.2.1 Synthesis of  $\text{Cu}_2\text{O}$  nanostructures.** The carbon paper was cut into pieces of size  $6 \text{ cm} \times 4 \text{ cm}$  and then gently (low power) sonicated in acetone and IPA for 5 minutes each to remove any unbound materials or surface impurities. The substrates were then dried with an  $\text{N}_2$  blower and heated at  $80^\circ \text{C}$  for 30 minutes to remove any solvent residue. After that,  $\text{Cu}_2\text{O}$  was sputter-deposited on the substrates. For sputtering, the base pressure of the deposition chamber was  $\sim 2 \times 10^{-7}$  torr, and the  $\text{Cu}_2\text{O}$  target was pre-sputtered for 30 min at 200 W. After that, the clean substrates were soaked at  $70^\circ \text{C}$  for 30 minutes inside the deposition chamber and then sputtered for 90 minutes at 200 W power (DC bias: 380 V), keeping the Ar and  $\text{O}_2$  flow fixed at 12 sccm and 0.3 sccm, respectively with a 3 mTorr chamber pressure during deposition.

**2.2.2 Plasma treatment.** The substrates were again cut into small pieces of size  $2 \text{ cm} \times 2 \text{ cm}$  and then treated with two different plasmas under different atmospheres, keeping all other parameters the same. For plasma treatment, the chamber was flushed with Ar gas three times before each treatment, and the chamber pressure was maintained at 100 mTorr and with an RIE and ICP power of 100 W each. Two different plasmas were created as per the set parameters with different gas flows as follows:  $\text{O}_2$  plasma:  $\text{O}_2$  flow 45 sccm, Ar flow 5 sccm; and  $\text{H}_2$  plasma:  $\text{H}_2$  flow 15 sccm, Ar flow 35 sccm.

### 2.3 Ex situ material characterization

Scanning electron microscopy (SEM, Hitachi S4800, Japan) images were taken with a working accelerating voltage of 10 kV. Glancing-incidence X-ray diffraction (GIXRD) spectra were collected on a MRD diffractometer (PANalytical X'Pert Pro, Netherlands) with Cu  $K\alpha$  radiation ( $1.54 \text{ \AA}$ ) at an incidence angle of  $0.3^\circ$ . X-ray photoelectron spectroscopy (XPS) measurements were conducted (Thermo-VG Scientific ESCALab 250, USA) using microprobes with a monochromatic Al  $K\alpha$  X-ray

source (1486.6 eV). High resolution TEM images (Zeiss Libra 200 MC, German) were collected with an acceleration voltage of 200 kV. The XAS measurements were conducted at the 06ID-1 Hard X-ray MicroAnalysis (HXMA) beamline of the Canadian Light Source (CLS) operated at 2.9 GeV with a constant current of 220 mA. The measurements at the copper K-edge were performed in fluorescence mode using a Ge detector. Proton nuclear magnetic resonance (H-NMR) spectroscopy was run on a Bruker Avance III 500 MHz, USA. The reduced products were evaluated on a gas chromatograph (Shimadzu, GC-2014) with a Carbonxen® 1000 column and a CarbonPLOT column for a flame ionization detector (FID) and thermal conductivity detector (TCD), respectively.

## 2.4 Electrochemical measurements

For the ECR test, all electrochemical tests were performed using an electrochemical workstation (Gamry Reference 3000) with *iR* compensation at room temperature. The performance evaluation of electrochemical CO<sub>2</sub> reduction is conducted in flow cell setups. A prepared sample on carbon paper, Ni foam, and Ag/AgCl are used as the working electrode, counter electrode, and reference electrode, respectively. A gas-tight three-chamber flow cell is equipped with a Fumasep FAB-PK-130 anion exchange membrane (AEM), and 1 M KOH serves as the cathode and anode circulating electrolyte with a flow rate of 18 mL min<sup>-1</sup>. The flow rate of CO<sub>2</sub> gas is set to 30 sccm. The ECR catalytic activities were evaluated using the potentiostatic technique for 1000 s. The gas products were analyzed using a Shimadzu GC-2014, while the liquid products were characterized using a Bruker 500 MHz Nuclear Magnetic Resonance (NMR) spectrometer with an internal reference prepared with D<sub>2</sub>O and DMSO.

All potentials in this work were measured against the Ag/AgCl reference electrode and converted into reversible hydrogen potential (RHE) using the equation below:

$$E(\text{vs. RHE}) = E(\text{vs. Ag/AgCl}) + 0.059 \times \text{pH} + 0.197$$

All the potentials are relative to the RHE unless stated otherwise.

## 2.5 DFT calculation details

All calculations were performed using the Vienna *ab initio* simulation package with the Perdew–Burke–Ernzerhof (PBE) generalized gradient approximation (GGA) exchange–correlation functional.<sup>30</sup> A plane wave cutoff energy of 450 eV was employed. Spin polarization and van der Waals corrections in the models were accounted for using the projector augmented wave (PAW)<sup>31</sup> method and DFT-D3,<sup>32</sup> respectively. The convergence criteria for the total energy and forces were set to  $1 \times 10^{-5}$  eV and  $0.03 \text{ eV } \text{\AA}^{-1}$ , respectively. The *k*-point sampling was performed using a  $3 \times 3 \times 1$  gamma scheme. A vacuum layer of 15 Å was introduced to eliminate interactions between the layers in the model. A three-layer Cu<sub>2</sub>O (111) surface was constructed to model the Cu<sub>2</sub>O sample, where the oxygen vacancy

on the Cu<sub>2</sub>O (111) surface is represented by removing a coordinated oxygen atom (Fig. S11a†). The Cu<sub>2</sub>O (111)/Cu (111) structure was obtained by adding two layers of Cu (111) under the Cu<sub>2</sub>O (111) surface, a four-layer slab model, to model the Cu<sub>2</sub>O–Ar/H<sub>2</sub> sample (Fig. S11b†). The VASPsol implicit solvation model was used to study the solvation effect.<sup>33</sup> As shown in Table S3†, taking two key intermediates of the potential-determining steps, \*CO and \*CHO, as examples, there is little difference in the reaction energies considering the solvation effect or not, and consequently the solvation effect is not considered.

# 3 Results and discussion

## 3.1 Synthesis and *ex situ* characterization of electrocatalysts

The material preparation process, involving both magnetron sputtering and plasma treatment, is illustrated in Fig. 1a. Initially, Cu<sub>2</sub>O catalysts are fabricated on a gas diffusion electrode (GDE) *via* magnetron sputtering using a Cu<sub>2</sub>O target. Subsequently, plasma treatments on Cu<sub>2</sub>O catalysts are conducted under reducing (Ar/H<sub>2</sub>) and oxidizing (Ar/O<sub>2</sub>) atmospheres, wherein highly reactive Ar/H<sub>2</sub> and Ar/O<sub>2</sub> active particles in the plasma state bombard the surface of Cu<sub>2</sub>O, causing further reduction or oxidation. This would create different structural defects in the resulting Cu<sub>2</sub>O–Ar/H<sub>2</sub> and Cu<sub>2</sub>O–Ar/O<sub>2</sub>. This facile and scalable material preparation method makes it feasible to produce large-scale gas diffusion electrode (GDE)-compatible high-activity ECR catalysts.

The composition and structural characteristics of the synthesized samples were investigated using grazing incidence X-ray diffraction (GIXRD). Diffraction peaks attributed to cuprite (Cu<sub>2</sub>O JCPDF#05-0667) are observed in the Cu<sub>2</sub>O and Cu<sub>2</sub>O–Ar/O<sub>2</sub> samples (Fig. 1b), indicating that Ar/O<sub>2</sub> plasma treatment does not reduce the original Cu<sub>2</sub>O. However, the mixed phase of Cu (JCPDF#04-0836) and Cu<sub>2</sub>O in the Cu<sub>2</sub>O–Ar/H<sub>2</sub> sample suggests that Ar/H<sub>2</sub> plasma treatment partially reduced Cu<sub>2</sub>O to metallic copper (Fig. 1b), forming interface structures between Cu and Cu<sub>2</sub>O. The scanning electron microscope (SEM) images reveal that Cu<sub>2</sub>O nanoparticles are *in situ* grown on carbon paper using magnetron sputtering (Fig. S1a and b†). The Ar/H<sub>2</sub> (Fig. 1c, d, S1c and d†) and Ar/O<sub>2</sub> (Fig. S1e and f†) plasma treatments do not visibly affect the morphology of Cu<sub>2</sub>O NPs. SEM-EDS elemental mapping images show a uniform distribution of Cu and O in the Cu<sub>2</sub>O (Fig. S2a†) and Cu<sub>2</sub>O–Ar/O<sub>2</sub> (Fig. S2b†) samples, while SEM-EDS images (Fig. 1e) confirm that Ar/H<sub>2</sub> plasma treatment does not completely reduce Cu<sub>2</sub>O to Cu, as oxygen signals are still detected. Correspondingly, in terms of elemental composition, compared to pristine Cu<sub>2</sub>O (Fig. S4†), the oxygen content in Cu<sub>2</sub>O–Ar/H<sub>2</sub> (Fig. S3†) is significantly reduced, while the oxygen content in Cu<sub>2</sub>O–Ar/O<sub>2</sub> (Fig. S5†) remains relatively unchanged. High-resolution transmission electron microscopy (HRTEM) images reveal the presence of abundant grain boundary structures in the as-synthesized samples (Fig. 1f and g). For the original Cu<sub>2</sub>O, lattice spacings of 0.29 nm and 0.24 nm are attributed to the (110) and (111) planes of Cu<sub>2</sub>O<sup>34</sup> (Fig. 1f and S6a and b†), respectively. However, after plasma



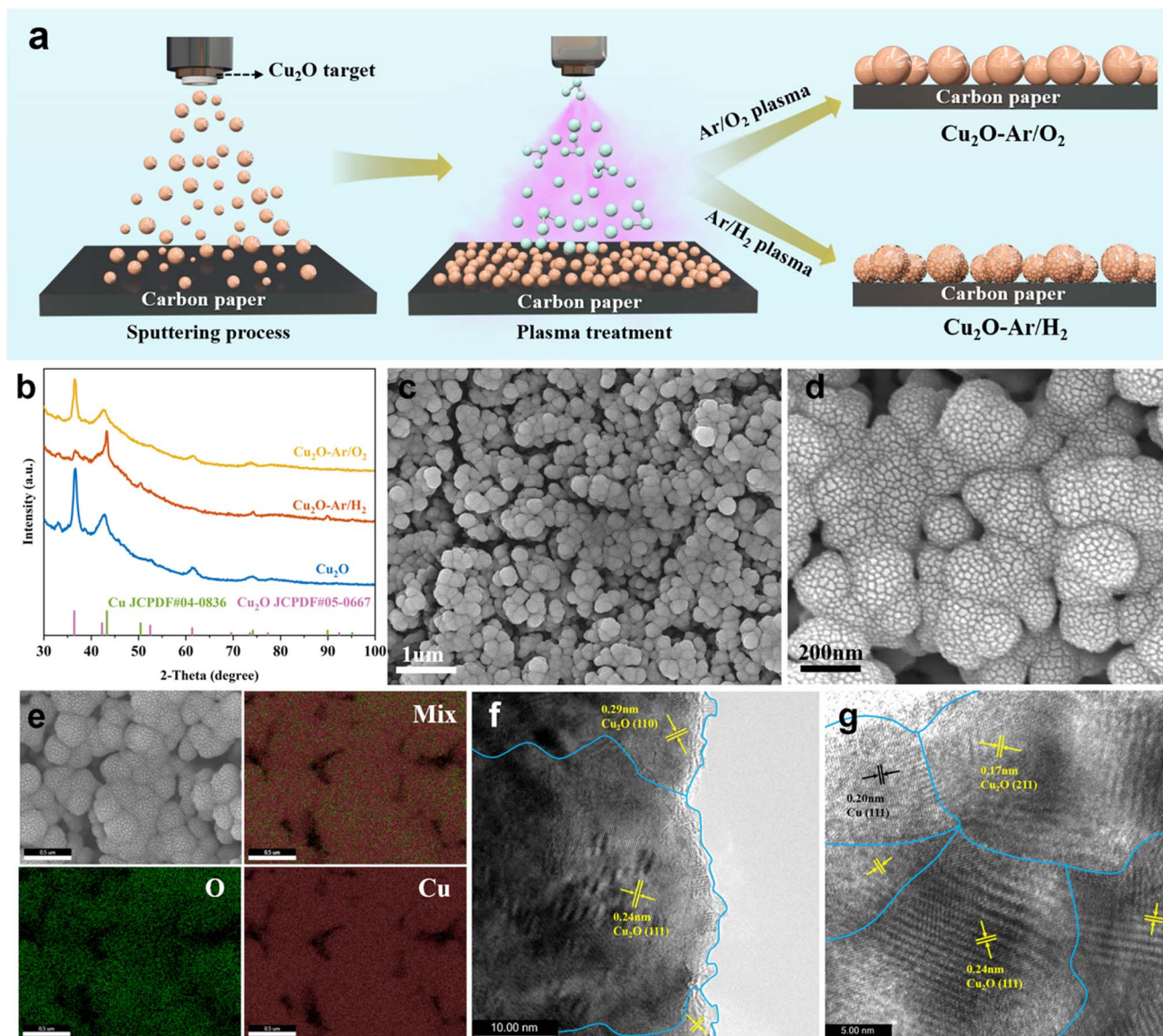


**Fig. 1** Synthesis and structural characterization of electrocatalysts. (a) The schematic illustration of the as-synthesized catalysts. (b) GIXRD spectra of the as-prepared electrocatalysts; (c and d) SEM images of  $\text{Cu}_2\text{O}-\text{Ar}/\text{H}_2$ ; (e) SEM-EDS elemental mapping images of  $\text{Cu}_2\text{O}-\text{Ar}/\text{H}_2$ ; (f and g) HRTEM images of  $\text{Cu}_2\text{O}$  (f) and  $\text{Cu}_2\text{O}-\text{Ar}/\text{H}_2$  (g).

reduction treatment on the  $\text{Cu}_2\text{O}-\text{Ar}/\text{H}_2$  sample, the grain boundary structures observed at 0.17 nm for  $\text{Cu}_2\text{O}$  (211), 0.20 nm for  $\text{Cu}$  (111), and 0.24 nm for  $\text{Cu}_2\text{O}$  (111) indicate the existence of  $\text{Cu}^0/\text{Cu}^+$  interface structures<sup>35,36</sup> (Fig. 1g and S7a†). This suggests that partial reduction of Cu atoms in  $\text{Cu}_2\text{O}$  nanoparticles has occurred under plasma reduction treatment, forming an interface between  $\text{Cu}^0$  and  $\text{Cu}^+$  within the  $\text{Cu}_2\text{O}$  lattice. Such interface structures may facilitate the formation of active sites and the generation of oxygen vacancies, thereby enhancing catalytic performance. In contrast, for the  $\text{Cu}_2\text{O}-\text{Ar}/\text{O}_2$  sample, only the grain boundary structures of  $\text{Cu}_2\text{O}$  (111) and (110) are observed, with no presence of metallic Cu (Fig. S7b†). This indicates that the plasma oxidation process does not create the unique interface structure seen in the  $\text{Cu}_2\text{O}-\text{Ar}/\text{H}_2$  sample.

X-ray photoelectron spectroscopy (XPS) was used to reveal changes in surface composition and chemical states of  $\text{Cu}_2\text{O}$  samples treated with plasma under different reaction atmospheres. For the  $\text{Cu}_2\text{O}$  and  $\text{Cu}_2\text{O}-\text{Ar}/\text{H}_2$  samples, the Cu 2p XPS spectrum can be deconvoluted into two peaks at 932.4 and 933.9 eV, corresponding to  $\text{Cu}^+/\text{Cu}^0$  and  $\text{Cu}^{2+}$  species<sup>21,37</sup> (Fig. S8†), respectively. However, compared to the samples treated with  $\text{Ar}/\text{H}_2$  plasma reduction, those treated with  $\text{Ar}/\text{O}_2$  plasma only exhibit features of  $\text{Cu}^{2+}$  species (Fig. S8†), indicating that the surface  $\text{Cu}_2\text{O}$  has been further oxidized. The Cu Auger LMM spectrum is employed to further confirm the valence state of the Cu species. For the original  $\text{Cu}_2\text{O}$  sample, the surface Cu is mainly in the monovalent and divalent Cu species.<sup>38</sup> After plasma reduction treatment, some of the surface Cu is reduced to metallic Cu,<sup>39</sup> showing the coexistence of zero-valent,

monovalent, and divalent Cu species (Fig. 2a). For Cu<sub>2</sub>O and Cu<sub>2</sub>O–Ar/H<sub>2</sub>, CuO originates from the inevitable oxidation of Cu species when exposed to air. Nevertheless, for Cu<sub>2</sub>O–Ar/O<sub>2</sub>, the presence of divalent copper on the surface results from the plasma oxidation treatment (Fig. 2a). Regarding the O 1s XPS spectrum, every O 1s curve is asymmetric and can be fitted into three components: lattice oxygen from Cu<sub>2</sub>O (O<sub>L</sub>(Cu<sup>+</sup>)) at 530.3 eV or CuO (O<sub>L</sub>(Cu<sup>2+</sup>)) at 529.5 eV,<sup>40</sup> adsorbed oxygen (O<sub>ad</sub>) at 531.5 eV, and adsorbed water (H<sub>2</sub>O<sub>ad</sub>) at 533.5 eV<sup>41,42</sup> (Fig. 2b). The ratio between O<sub>ad</sub> and O<sub>L</sub> can be used to evaluate the amount of surface oxygen vacancies.<sup>43</sup> It can be observed that the oxygen vacancy content follows this order: Cu<sub>2</sub>O–Ar/H<sub>2</sub> (3.95) > Cu<sub>2</sub>O (2.54) > Cu<sub>2</sub>O–Ar/O<sub>2</sub> (0.97), indicating that Cu<sub>2</sub>O–Ar/H<sub>2</sub> has a higher density of surface oxygen vacancies compared to its other two counterparts.

Synchrotron-based X-ray absorption Near-Edge Structure (XANES) spectra and Extended X-ray Absorption Fine Structure (EXAFS) spectra were recorded to further study the chemical state and local coordination environment of copper sites. Compared to Cu<sub>2</sub>O and CuO references, the XANES spectra of the as-synthesized samples display characteristics of Cu<sub>2</sub>O (Fig. 2c). Although plasma reduction or oxidation treatments could affect the oxidation state of surface Cu atoms, the bulk phase of the catalysts retains attributes of Cu<sub>2</sub>O. On the other

hand, fitting in the *R*-space of EXAFS spectra of the as-prepared samples was then conducted to quantify changes in scattering paths (Fig. 2d and Table S1†). For the original Cu<sub>2</sub>O sample, a Cu–O coordination number of 1.90 at 1.84 Å and Cu–Cu coordination number of 13.1 at 3.01 Å can be observed, similar to the Cu<sub>2</sub>O reference, indicating the characteristic properties of Cu<sub>2</sub>O. After plasma reduction or oxidation treatment, different Cu–O coordination numbers of 1.77 at 1.79 Å for Cu<sub>2</sub>O–Ar/H<sub>2</sub> and 1.65 at 1.84 Å for Cu<sub>2</sub>O–Ar/O<sub>2</sub> can be obtained, indicating that plasma treatment results in structural changes around Cu. For Cu<sub>2</sub>O–Ar/H<sub>2</sub>, the reduced Cu–O coordination number and similar Cu–Cu coordination number compared to the Cu<sub>2</sub>O reference indicate the presence of oxygen vacancies. A wavelet transform was employed to elucidate the coordination environment near the Cu atoms and confirm the atomic distribution of Cu in all samples. As shown in Fig. 2e, for the Cu<sub>2</sub>O reference, a strong wavelet transform signal focused at around 5 Å<sup>−1</sup> originating from Cu–O coordination is observed, while another intense signal at the same focus can be attributed to Cu–Cu coordination. The wavelet transform contour plot of the CuO reference exhibits only Cu–O coordination features (Fig. S9a†). In contrast, the original Cu<sub>2</sub>O sample exhibits similar peak intensities and positions to the Cu<sub>2</sub>O reference (Fig. S9b†), indicating their resemblance in structures.

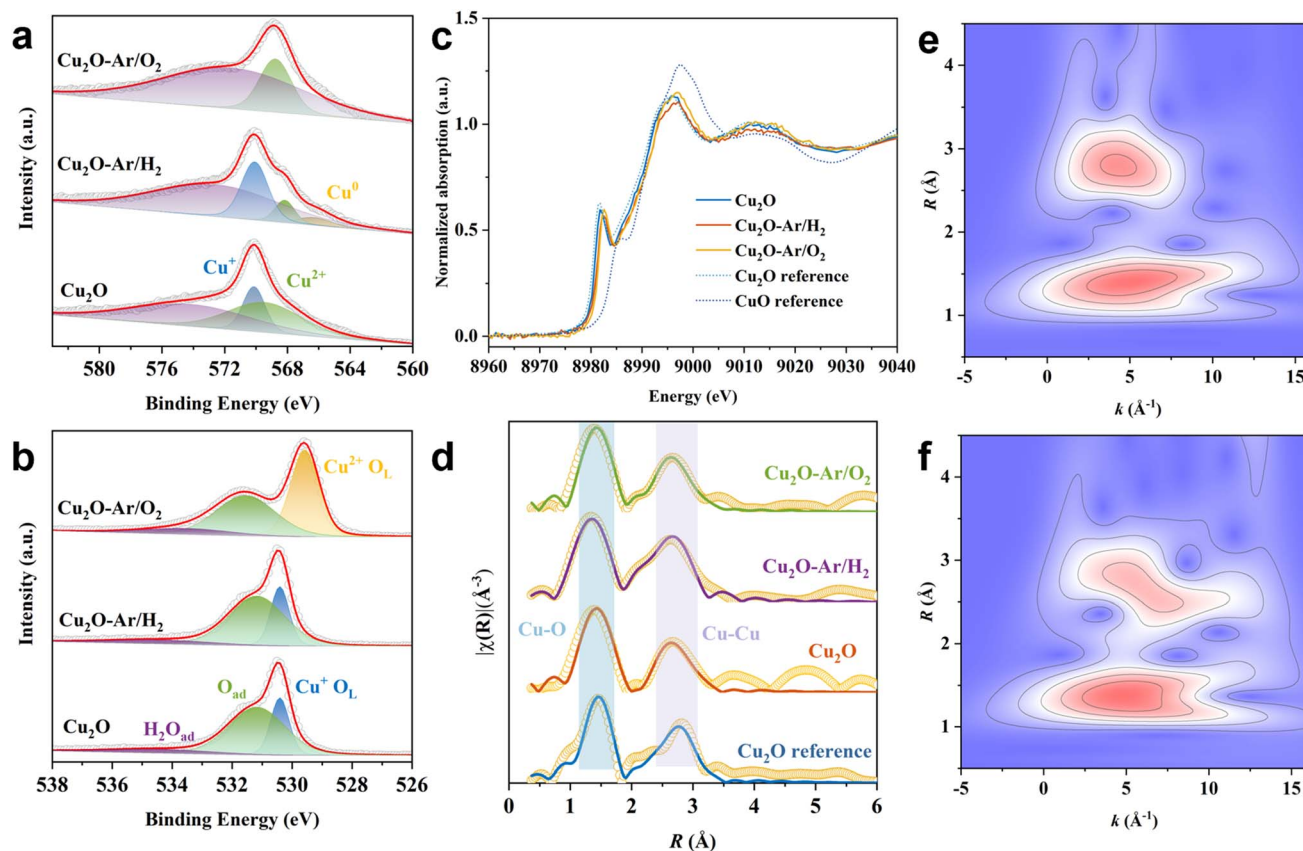


Fig. 2 *Ex situ* X-ray spectroscopic analysis of electrocatalysts. (a and b) Cu LMM Auger spectra (a) and O 1s XPS spectra (b) of the as-prepared catalysts; (c) Cu K-edge XANES spectra of Cu<sub>2</sub>O, Cu<sub>2</sub>O–Ar/H<sub>2</sub> and Cu<sub>2</sub>O–Ar/O<sub>2</sub> samples and corresponding references (Cu<sub>2</sub>O, and CuO). (d) Cu K-edge EXAFS experimental and fitting spectra of Cu<sub>2</sub>O, Cu<sub>2</sub>O–Ar/H<sub>2</sub> and Cu<sub>2</sub>O–Ar/O<sub>2</sub> catalysts and corresponding references (Cu<sub>2</sub>O). (e and f) Wavelet transforms for the *k*<sup>3</sup>-weighted EXAFS signals of Cu<sub>2</sub>O reference (e) and Cu<sub>2</sub>O–Ar/H<sub>2</sub> (f).

However, after plasma reduction or oxidation treatment, differing first shell Cu–O and second shell Cu–Cu scattering distributions suggest variations in the local coordination environment around Cu between Cu<sub>2</sub>O–Ar/H<sub>2</sub> and Cu<sub>2</sub>O–Ar/O<sub>2</sub> (Fig. 2f vs. Fig. S9c†).

### 3.2 Electrochemical CO<sub>2</sub> reduction performance

The ECR performance of the as-synthesized catalysts was evaluated in a flow cell using an alkaline electrolyte (1 M KOH). All catalysts exhibit a similar reduced product distribution, with CO, methane, and formic acid as the main C<sub>1</sub> products and ethylene, ethanol, acetic acid, and isopropanol as the main C<sub>2+</sub> products (Fig. 3a, S10a and b†). For all samples, the H<sub>2</sub> FE increases with increasing cathodic potentials, suggesting that at higher negative potentials, the competitive hydrogen evolution reaction (HER) suppresses the production of C<sub>2+</sub> products. Therefore, all samples demonstrate higher C<sub>2+</sub> product selectivity at lower potentials (−0.65 or −0.7 V<sub>RHE</sub>). The Cu<sub>2</sub>O sample shows a relatively high C<sub>2+</sub> FE (70.47%) at −0.65 V<sub>RHE</sub>, but as the potentials increase, the C<sub>2+</sub> FE continues to decrease to 39% at −0.75 V<sub>RHE</sub> (Fig. 3b). Increasing the cathode potentials induces the further reduction of Cu<sub>2</sub>O to metallic Cu. Since oxidative Cu species act as

the main active sites for C<sub>2+</sub> products, the reduction in these active species on the catalyst surface results in a decrease in the selectivity for C<sub>2+</sub> products. This indicates that *in situ* reduction of Cu<sub>2</sub>O cannot enhance catalytic activity at higher cathodic potentials, possibly due to the inherent Cu<sub>2</sub>O grain boundary structure's inability to stabilize active Cu<sup>+</sup> species. Although plasma oxidation treatment (Ar/O<sub>2</sub>) raises the oxidation state of Cu<sub>2</sub>O, achieving a C<sub>2+</sub> FE of 77.14% at low potential (−0.65 V<sub>RHE</sub>), it still fails to stabilize active Cu<sup>+</sup> species at higher potentials (−0.7 and −0.75 V<sub>RHE</sub>), leading to decreased activity (Fig. 3b). However, for the Cu<sub>2</sub>O–Ar/H<sub>2</sub> sample, the C<sub>2+</sub> FE is lower than that of Cu<sub>2</sub>O and Cu<sub>2</sub>O–Ar/O<sub>2</sub> at −0.65 V<sub>RHE</sub>, but at −0.7 V<sub>RHE</sub>, the C<sub>2+</sub> FE reaches 81.2% with a current density of ~100 mA cm<sup>−2</sup>. Moreover, at higher potentials (−0.75 V<sub>RHE</sub>), the C<sub>2+</sub> FE of Cu<sub>2</sub>O–Ar/H<sub>2</sub> also exceeds that of Cu<sub>2</sub>O and Cu<sub>2</sub>O–Ar/O<sub>2</sub> (Fig. 3b). This suggests that the Cu<sup>0</sup>/Cu<sup>+</sup> interface structure and high density of oxygen vacancies obtained through plasma reduction treatment (Ar/H<sub>2</sub>) can effectively stabilize active Cu species during ECR, enhancing C<sub>2+</sub> selectivity. Considering the impact of plasma treatment on catalytic activity of C<sub>2+</sub> products, a comparison is made with other plasma-treated catalysts in terms of C<sub>2+</sub> FE (Fig. 3c and Table S2†). The results show that catalytic activity

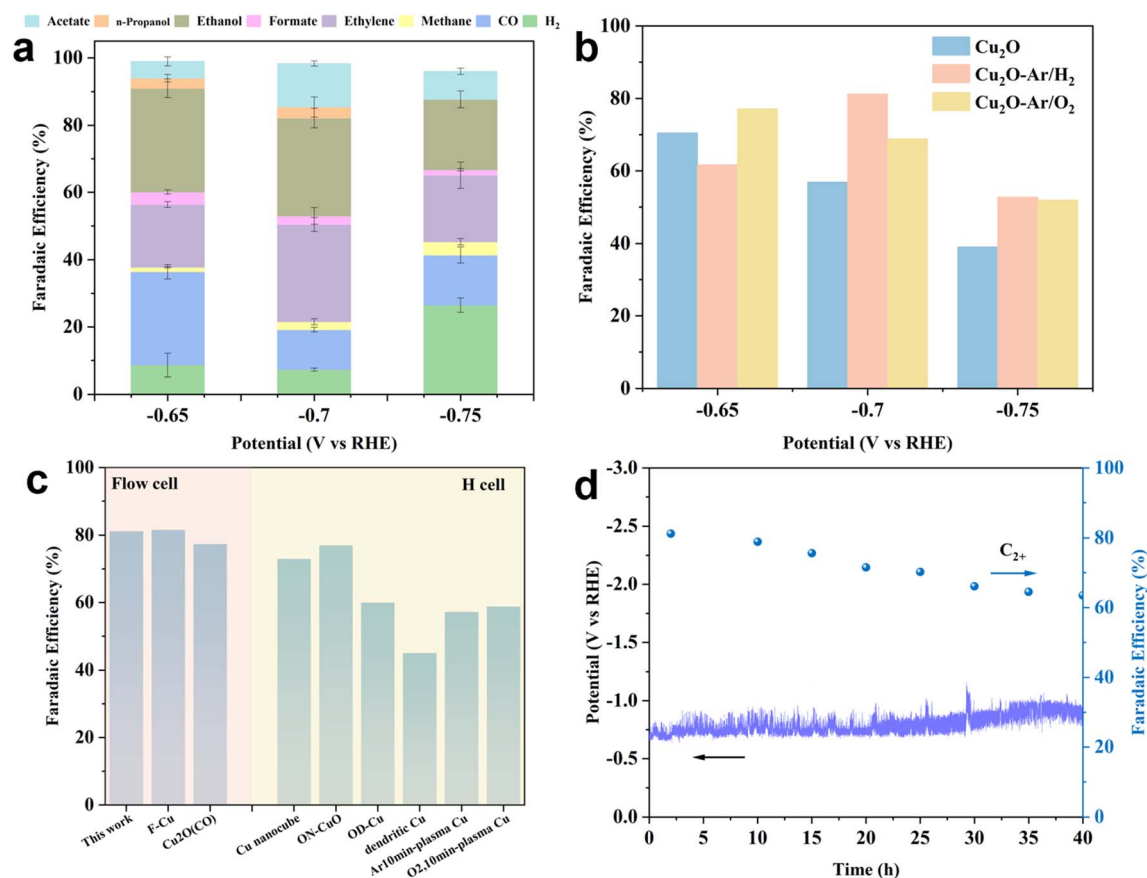


Fig. 3 ECR performance of the as-prepared catalysts. (a) The reduced product distribution of CO<sub>2</sub> for Cu<sub>2</sub>O–Ar/H<sub>2</sub> at different cathodic potentials under ECR. (b) The FEs for C<sub>2+</sub> products on the as-synthesized samples. (c) Comparisons of the FE values for C<sub>2+</sub> products between Cu<sub>2</sub>O–Ar/H<sub>2</sub> and other recently reported plasma-treated Cu-based catalysts. The summary of the specific ECR performance of catalysts is presented in Table S1.† (d) The stability test of Cu<sub>2</sub>O–Ar/H<sub>2</sub> at a current density of 100 mA cm<sup>−2</sup> using a flow cell.



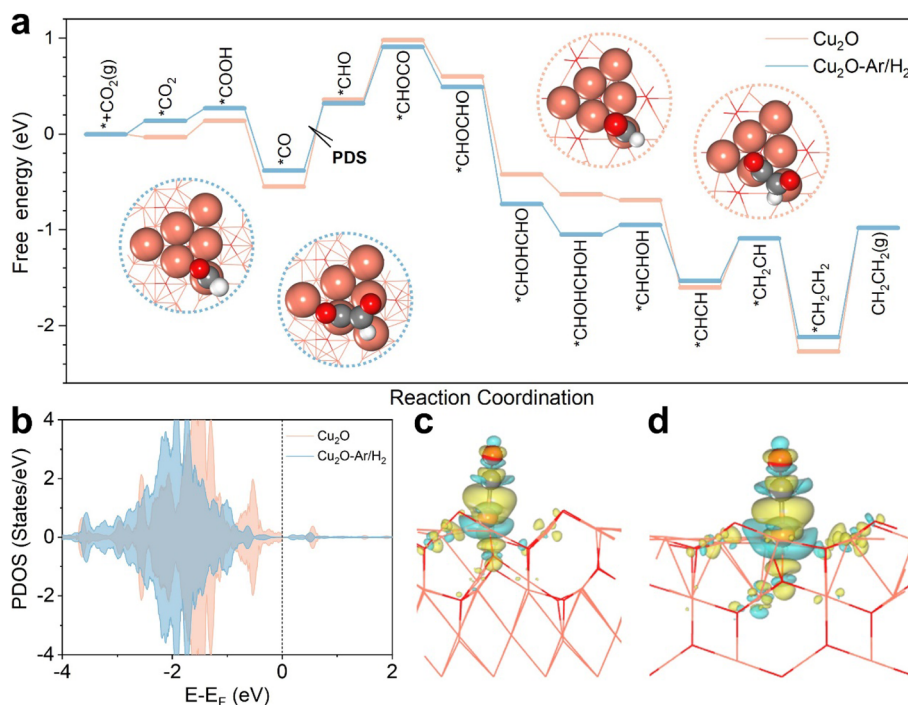


Fig. 4 DFT investigations. (a) Free energy profile of ethylene production on Cu<sub>2</sub>O-Ar/H<sub>2</sub> and Cu<sub>2</sub>O, including the \*CHO and \*CHOCO structures. (b) PDOS of the Cu-d states of vertex Cu atoms in Cu<sub>2</sub>O-Ar/H<sub>2</sub> and Cu<sub>2</sub>O. Charge density differences of \*CO on (c) Cu<sub>2</sub>O-Ar/H<sub>2</sub> and (d) Cu<sub>2</sub>O with an isovalue of 0.001 e Å<sup>-3</sup>, where yellow and cyan regions denote electron accumulation and depletion, respectively.

of Cu<sub>2</sub>O-Ar/H<sub>2</sub> exceeds that of most plasma-treated samples, demonstrating excellent ECR performance in terms of the C<sub>2+</sub> product pathway.

A long-term stability test was conducted to evaluate the practical applicability of the catalyst. Considering the C<sub>2+</sub> product selectivity and industrial-relevant current densities, Cu<sub>2</sub>O-Ar/H<sub>2</sub> was selected to run stability tests in a flow cell with 1 M KOH at a constant current of 100 mA cm<sup>-2</sup> (Fig. 3d). The results show that the ECR system could operate stably for 40 h, with a gradual decrease in C<sub>2+</sub> FE from an initial 81.2% to 63.5%. This indicates that Cu<sub>2</sub>O-Ar/H<sub>2</sub> has significant potential for industrial-scale ECR to C<sub>2+</sub> product conversion as it can be used as a standardized process.

### 3.3 DFT calculations

To better understand how interface structures and oxygen vacancies enhance the activity towards C<sub>2+</sub> products, we conducted DFT calculations with ethylene as the representative C<sub>2+</sub> product. As shown in Fig. S11,<sup>†</sup> there are Cu triangles due to oxygen vacancies, of which both vertex and edge Cu atoms can be active sites. The project density of states (PDOS) shows that the Cu-d states of vertex atoms are always closer to the Fermi level than those of edge atoms (Fig. S12<sup>†</sup>), so CO<sub>2</sub> adsorption begins on these sites. For ethylene production, the adsorbed \*CO<sub>2</sub> is reduced to \*CO first and then hydrogenated to \*CHO on vertex Cu atoms, and subsequently the C-C coupling occurs, \*CHO + \*CO → \*CHOCO, on both vertex and edge Cu atoms (Fig. 4a). The C-C coupling step is always endothermic but is weaker than the hydrogenation of \*CO to \*CHO, and the

potential-determining step (PDS) is thus \*CO → \*CHO, with the free energy changes of the PDS of 0.70 and 0.91 eV for Cu<sub>2</sub>O-Ar/H<sub>2</sub> and Cu<sub>2</sub>O, respectively. Fig. 4b shows the PDOS of vertex Cu atoms in Cu<sub>2</sub>O-Ar/H<sub>2</sub> and Cu<sub>2</sub>O, and we can find that the Cu-d states of Cu<sub>2</sub>O-Ar/H<sub>2</sub> are more far to the Fermi level than those of Cu<sub>2</sub>O, which leads to different adsorption strengths of \*CO. Electron accumulation between active Cu sites and the C atom of \*CO can be found in the charge density difference plots (Fig. 4c and d), validating strong interactions between \*CO and catalysts. The Bader charge analysis suggests that 0.10 |e| is transferred from Cu<sub>2</sub>O-Ar/H<sub>2</sub> to \*CO, which is smaller than that on Cu<sub>2</sub>O (0.16 |e|), in accordance with the more unactive Cu-d states of Cu<sub>2</sub>O-Ar/H<sub>2</sub> shown in Fig. 4b. This leads to weaker \*CO adsorption on Cu<sub>2</sub>O-Ar/H<sub>2</sub> with E<sub>ads-CO</sub> = -1.58 eV, while E<sub>ads-CO</sub> = -1.83 eV for Cu<sub>2</sub>O. In short, multiple active sites induced by oxygen vacancies make the C-C coupling easier than the \*CO hydrogenation and weaker \*CO adsorption on Cu<sub>2</sub>O-Ar/H<sub>2</sub> related to interface engineering makes the \*CO hydrogenation easier than that on Cu<sub>2</sub>O.

## 4 Conclusions

In summary, a facile, scalable, and standardized magnetron sputtering method combined with plasma surface treatment was developed to controllably construct high-activity catalysts for C<sub>2+</sub> products. Cu<sub>2</sub>O with rich grain boundaries, upon plasma reduction treatment, displays a well-defined Cu<sup>0</sup>/Cu<sup>+</sup> interface structure with abundant oxygen vacancies. The enhanced activity stems from the synergistic interaction of the interface

structure and oxygen vacancies. Compared to the original  $\text{Cu}_2\text{O}$  and  $\text{Cu}_2\text{O}$  further treated with plasma oxidation, pre-plasma reduction treatment of  $\text{Cu}_2\text{O}$  effectively prevents the loss of active sites during *in situ* reduction of ECR. This work reveals the real active sites created by plasma treatment during the ECR process, effectively promoting the industrial-scale application of ECR.

## Data availability

The authors declare that all data supporting this study are available within the paper and ESI† files. Source data are provided upon request.

## Author contributions

Y. A. W. conceived and supervised the project. Z. T. co-supervised the project. C. V. S. and L. Z. led the DFT calculations. S. J. and Y. Z. carried out the catalyst's synthesis. L. W. conducted characterization and performance tests of catalysts. X. Y. and C. Q. conducted the DFT calculations. S. J. carried out the XAS measurements. N. C. provided advice for the XAFS measurements. L. W., X. Y., S. J., C. V. S., Z. C. T., and Y. A. W. wrote the manuscript. All authors made comments and revised the manuscript.

## Conflicts of interest

All the authors declare no competing interests.

## Acknowledgements

Y. A. W. acknowledges the funding from the Government of Canada's New Frontiers Research Fund-Transformation CAN-STOREnergy Project (NFRFT-2022-00197), the Natural Sciences and Engineering Research Council of Canada (NSERC) (RGPIN-2020-05903 and GECR-2020-00476), the Tang Family Chair in New Energy Materials and Sustainability, the Canadian Foundation for Innovation John R. Evans Leaders Fund (#41779), and the Ontario Research Fund for Small Infrastructure (#41779). Z. T. acknowledges the funding from the NSERC collaborative research and training experience program (CREATE) and GCI Ventures Capital, Toronto. This research used the resources of the Canadian Light Source and its funding partners. The studies for hard XAS were performed at HXMA beamlines of the Canadian Light Source (CLS), a national research facility of the University of Saskatchewan, which is supported by the Canada Foundation for Innovation (CFI), the Natural Sciences and Engineering Research Council (NSERC), the National Research Council (NRC), the Canadian Institutes of Health Research (CIHR), and the Government of Saskatchewan. C. V. S. acknowledges support of the Natural Sciences & Engineering Research Council of Canada (NSERC), University of Toronto, and the Digital Research Alliance of Canada for enabling DFT simulations.

## References

- 1 C. P. O'Brien, *et al.*,  $\text{CO}_2$  Electrolyzers, *Chem. Rev.*, 2024, **124**, 3648–3693.
- 2 L. Peng, *et al.*, Research advances in electrocatalysts, electrolytes, reactors and membranes for the electrocatalytic carbon dioxide reduction reaction, *Acta Phys.-Chim. Sin.*, 2023, **39**(12), 2302037.
- 3 Y. Jia, *et al.*, Cu-based bimetallic electrocatalysts for  $\text{CO}_2$  reduction, *Adv. Powder Mater.*, 2022, **1**(1), 100012.
- 4 L. Fan, *et al.*, Strategies in catalysts and electrolyzer design for electrochemical  $\text{CO}_2$  reduction toward  $\text{C}_{2+}$  products, *Sci. Adv.*, 2020, **6**(8), eaay3111.
- 5 L. Fan, *et al.*, 1D  $\text{SnO}_2$  with Wire-in-Tube Architectures for Highly Selective Electrochemical Reduction of  $\text{CO}_2$  to  $\text{C}_1$  Products, *Adv. Funct. Mater.*, 2018, **28**(17), 1706289.
- 6 S. Verma, *et al.*, The effect of electrolyte composition on the electroreduction of  $\text{CO}_2$  to CO on Ag based gas diffusion electrodes, *Phys. Chem. Chem. Phys.*, 2016, **18**(10), 7075–7084.
- 7 W. Ma, *et al.*, Electrocatalytic reduction of  $\text{CO}_2$  and CO to multi-carbon compounds over Cu-based catalysts, *Chem. Soc. Rev.*, 2021, **50**(23), 12897–12914.
- 8 M. Ma, *et al.*, Controllable hydrocarbon formation from the electrochemical reduction of  $\text{CO}_2$  over Cu nanowire arrays, *Angew. Chem. Int. Ed.*, 2016, **55**(23), 6680–6684.
- 9 C. W. Li, *et al.*, Electroreduction of carbon monoxide to liquid fuel on oxide-derived nanocrystalline copper, *Nature*, 2014, **508**(7497), 504–507.
- 10 X. Chang, *et al.*, Tuning Cu/ $\text{Cu}_2\text{O}$  interfaces for the reduction of carbon dioxide to methanol in aqueous solutions, *Angew. Chem.*, 2018, **130**(47), 15641–15645.
- 11 X. Y. Zhang, *et al.*, Direct OC-CHO coupling towards highly  $\text{C}_{2+}$  products selective electroreduction over stable  $\text{Cu}^0/\text{Cu}^{2+}$  interface, *Nat. Commun.*, 2023, **14**(1), 7681.
- 12 W. J. Dong, *et al.*, Grain Boundary Engineering of Cu-Ag Thin-Film Catalysts for Selective (Photo) Electrochemical  $\text{CO}_2$  Reduction to CO and  $\text{CH}_4$ , *ACS Appl. Mater. Interfaces*, 2021, **13**(16), 18905–18913.
- 13 Z. Chang, *et al.*, The tunable and highly selective reduction products on Ag@Cu bimetallic catalysts toward  $\text{CO}_2$  electrochemical reduction reaction, *J. Phys. Chem. C*, 2017, **121**(21), 11368–11379.
- 14 J. Chen and L. Wang, Effects of the catalyst dynamic changes and influence of the reaction environment on the performance of electrochemical  $\text{CO}_2$  reduction, *Adv. Mater.*, 2022, **34**(25), 2103900.
- 15 Q. Wu, *et al.*, Nanograin-Boundary-Abundant  $\text{Cu}_2\text{O}$ -Cu Nanocubes with High  $\text{C}_{2+}$  Selectivity and Good Stability during Electrochemical  $\text{CO}_2$  Reduction at a Current Density of  $500 \text{ mA cm}^{-2}$ , *ACS Nano*, 2023, **17**, 12884–12894.
- 16 Y. Yang, *et al.*, Operando studies reveal active Cu nanograins for  $\text{CO}_2$  electroreduction, *Nature*, 2023, **614**(7947), 262–269.
- 17 X. Yuan, *et al.*, Controllable  $\text{Cu}^0$ - $\text{Cu}^+$  sites for electrocatalytic reduction of carbon dioxide, *Angew. Chem.*, 2021, **133**(28), 15472–15475.



- 18 H. Li, *et al.*, Oxygen vacancy structure associated photocatalytic water oxidation of BiOCl, *ACS Catal.*, 2016, **6**(12), 8276–8285.
- 19 H. Li, *et al.*, Oxygen vacancy-mediated photocatalysis of BiOCl: reactivity, selectivity, and perspectives, *Angew. Chem. Int. Ed.*, 2018, **57**(1), 122–138.
- 20 X. Li, *et al.*, Strategies for enhancing electrochemical CO<sub>2</sub> reduction to multi-carbon fuels on copper, *Innov. Mater.*, 2023, **1**(1), 100014.
- 21 Z. Gu, *et al.*, Oxygen vacancy tuning toward efficient electrocatalytic CO<sub>2</sub> reduction to C<sub>2</sub>H<sub>4</sub>, *Small Methods*, 2019, **3**(2), 1800449.
- 22 Y. Wang, *et al.*, Defect and interface engineering for aqueous electrocatalytic CO<sub>2</sub> reduction, *Joule*, 2018, **2**(12), 2551–2582.
- 23 J.-J. Zou, *et al.*, Control of the metal – support interface of NiO-loaded photocatalysts *via* cold plasma treatment, *Langmuir*, 2006, **22**(5), 2334–2339.
- 24 D. G. Park, *et al.*, Increasing CO binding energy and defects by preserving Cu oxidation state *via* O<sub>2</sub>-plasma-assisted N doping on CuO enables high C<sub>2+</sub> selectivity and long-term stability in electrochemical CO<sub>2</sub> reduction, *ACS Catal.*, 2023, **13**(13), 9222–9233.
- 25 Y. Zhou, *et al.*, Dopant-induced electronic structure modification of HOPG surfaces: implications for high activity fuel cell catalysts, *J. Phys. Chem. C*, 2010, **114**(1), 506–515.
- 26 H. Mistry, *et al.*, Highly selective plasma-activated copper catalysts for carbon dioxide reduction to ethylene, *Nat. Commun.*, 2016, **7**(1), 1–9.
- 27 D. Gao, *et al.*, Plasma-activated copper nanocube catalysts for efficient carbon dioxide electroreduction to hydrocarbons and alcohols, *ACS Nano*, 2017, **11**(5), 4825–4831.
- 28 P. Chen, *et al.*, *In situ* reconfiguration of plasma-engineered copper electrodes towards efficient electrocatalytic hydrogenation, *Catal. Sci. Technol.*, 2022, **12**(12), 4032–4039.
- 29 F. Scholten, *et al.*, Plasma-modified dendritic Cu catalyst for CO<sub>2</sub> electroreduction, *ACS Catal.*, 2019, **9**(6), 5496–5502.
- 30 J. P. Perdew, *et al.*, Generalized Gradient Approximation Made Simple, *Phys. Rev. Lett.*, 1996, **77**(18), 3865–3868.
- 31 G. Kresse and J. Furthmüller, Efficiency of *ab initio* total energy calculations for metals and semiconductors using a plane-wave basis set, *Comput. Mater. Sci.*, 1996, **6**(1), 15–50.
- 32 S. Grimme, *et al.*, A consistent and accurate *ab initio* parametrization of density functional dispersion correction (DFT-D) for the 94 elements H–Pu, *J. Chem. Phys.*, 2010, **132**(15), 154104.
- 33 K. Mathew, *et al.*, Implicit solvation model for density-functional study of nanocrystal surfaces and reaction pathways, *J. Chem. Phys.*, 2014, **140**, 084106.
- 34 C. Chen, *et al.*, The *in situ* study of surface species and structures of oxide-derived copper catalysts for electrochemical CO<sub>2</sub> reduction, *Chem. Sci.*, 2021, **12**(16), 5938–5943.
- 35 Z. Zhou, *et al.*, Enhanced CO<sub>2</sub> Electroreduction to Multi-Carbon Products on Copper *via* Plasma Fluorination, *Adv. Sci.*, 2024, 2309963.
- 36 C. Ma, *et al.*, A novel core/shell cuprous oxide-based structure with improved microwave absorbing and antibacterial performance, *J. Clean. Prod.*, 2022, **378**, 134419.
- 37 Y.-H. Zhang, *et al.*, Oxygen vacancies in concave cubes Cu<sub>2</sub>O-reduced graphene oxide heterojunction with enhanced photocatalytic H<sub>2</sub> production, *J. Mater. Sci.: Mater. Electron.*, 2019, **30**, 7182–7193.
- 38 I. Platzman, *et al.*, Oxidation of polycrystalline copper thin films at ambient conditions, *J. Phys. Chem. C*, 2008, **112**(4), 1101–1108.
- 39 Y. Yang, *et al.*, Nitrogen-doping boosts \*CO utilization and H<sub>2</sub>O activation on copper for improving CO<sub>2</sub> reduction to C<sub>2+</sub> products, *Green Energy Environ.*, 2023, in press.
- 40 Y. Wang, *et al.*, Synthesis of porous Cu<sub>2</sub>O/CuO cages using Cu-based metal-organic frameworks as templates and their gas-sensing properties, *J. Mater. Chem. A*, 2015, **3**(24), 12796–12803.
- 41 L. Xue, *et al.*, Unveiling the reaction pathway on Cu/CeO<sub>2</sub> catalyst for electrocatalytic CO<sub>2</sub> reduction to CH<sub>4</sub>, *Appl. Catal., B*, 2022, **304**, 120951.
- 42 Q. T. Trinh, *et al.*, Synergistic application of XPS and DFT to investigate metal oxide surface catalysis, *J. Phys. Chem. C*, 2018, **122**(39), 22397–22406.
- 43 Z. Wang, *et al.*, Surface oxygen vacancies on Co<sub>3</sub>O<sub>4</sub> mediated catalytic formaldehyde oxidation at room temperature, *Catal. Sci. Technol.*, 2016, **6**(11), 3845–3853.